Source Parameters of Three Moderate Size Earthquakes in Weiyuan, China, and Their Relations to Shale Gas Hydraulic Fracturing

Minhan Sheng[1,2]**, Risheng Chu**[1,2] (iD)**, Sidao Ni**[1,2] (iD)**, Yong Wang**[1,2]**, Liming Jiang**[1,2]**, and Hongfeng Yang**[3] (iD)

[1]State Key Laboratory of Geodesy and Earth's Dynamics, Innovation Academy for Precision Measurement Science and Technology, Chinese Academy of Sciences, Wuhan, China, [2]University of Chinese Academy of Sciences, Beijing, China, [3]Earth System Science Program, The Chinese University of Hong Kong, Hong Kong

Abstract On 7 September 2019, an M_L 5.4 earthquake struck the Weiyuan area in southwestern China. This is the largest and most damaging event in the Weiyuan shale gas field. In the next 4 months, two earthquakes with M_L 4.3 and M_L 5.2 rattled the same area. In this study, we obtain source parameters of these earthquakes (e.g., centroid location, focal mechanism, and rupture directivity) to investigate whether they are induced by hydraulic fracturing of shale gas production. We first invert for high-resolution centroid locations and focal mechanisms of two $M \sim 3$ earthquakes recorded by a temporary dense seismic array. We then adopt the $M \sim 3$ events as references to obtain reliable centroid locations and rupture directivity of those moderate-size earthquakes. The results show that all earthquakes have centroid depths of no more than 3 km and are within 2 km to injection wells of shale gas production, which suggest that these earthquakes may be induced by local hydraulic fracturing. The M_L 5.2 earthquake has the same rupture directivity to NE as the M_L 5.4 event and is located in the zone of positive Coulomb stress change caused by the latter. However, the long time lapse of the M_L 5.2 earthquake and the existence of an injection well within 2 km suggest that it is more likely induced by hydraulic fracturing than triggered statically by the M_L 5.4 earthquake.

1. Introduction

Earthquake hypocenters (i.e., epicenters and depths) are critical parameters for discriminating induced seismicity from natural earthquakes (Davis & Frohlich, 1993; Grigoli et al., 2018). The depths of natural tectonic earthquakes are mostly concentrated at about 10–20 km (Brantut & Platt, 2017; Marone & Scholz, 1988; Wang & Chu, 2020). However, induced earthquakes usually occur at depths of a few kilometers, which are caused by hydraulic fracturing or waste water injection due to various mechanisms (Ellsworth, 2013; Weingarten et al., 2015; Yeck et al., 2016). Induced earthquakes would most likely occur close to the injection wells at similar depths if the injected fluid flows along approximately horizontal strata. Therefore, another criterion to identify induced earthquakes is whether the epicenter of an earthquake is located near injection wells, usually within 5 km (Davis & Frohlich, 1993). In some cases, stress perturbations from large-volume wells or sets of wells can even induce earthquakes with distances of tens of kilometers in regions of high permeability (Keranen & Weingarten, 2018; Keranen et al., 2014; King et al., 2014).

In the midwestern United States, most earthquakes are induced by waste water disposal (Rubinstein & Mahani, 2015), and majority of these earthquakes have strike-slip focal mechanisms (Chen, Haffener, et al., 2018; McNamara et al., 2015). Induced earthquakes in central Alberta also exhibit a preference for strike-slip motions (Schultz et al., 2017). There are less studies on induced earthquakes in regions with compressional stress and thrusting faults, such as the Sichuan Basin (Figure 1), where the Tibetan plateau collides with the Eurasian plate (Hubbard & Shaw, 2009).

On the western edge of the Sichuan Basin, natural earthquakes in the Longmengshan fault zone are mostly distributed in a depth of 5–20 km (Huang et al., 2008). However, the interior of the basin just begins to witness some damaging earthquakes in recent years, which are proposed to be related to human activities (Lei et al., 2017, 2019, 2020; Liu & Zahradník, 2020; Luo et al., 2011; Qian et al., 2019; Sun et al., 2017). For example, several moderate-size earthquakes rattled the Changning-Weiyuan National Shale Gas
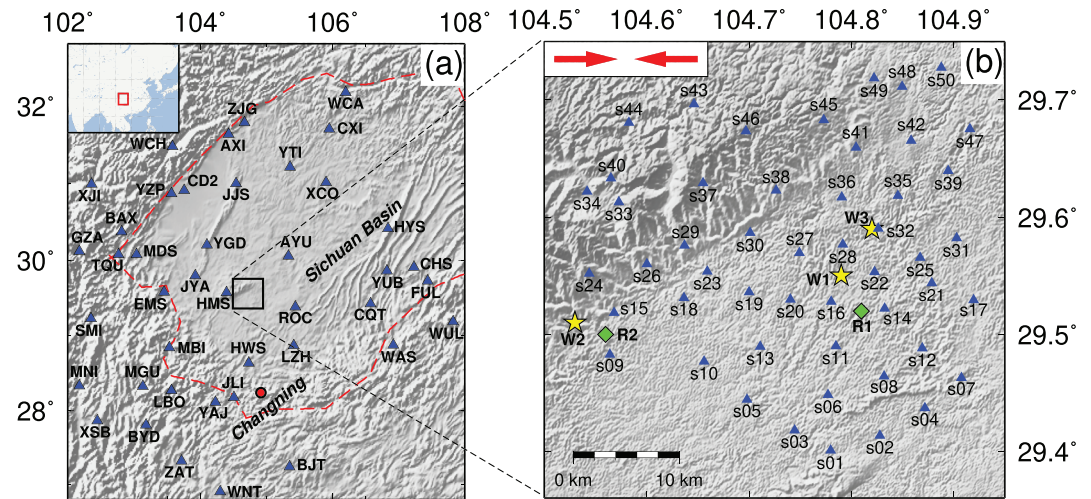
Figure 1. Broadband seismic stations and earthquakes used in this study. (a) Blue triangles and red dot are permanent stations and the 2018 Changning earthquake in the Sichuan Basin. The black box shows location of the study area. Red dashed lines enclose the Sichuan Basin. (b) Blue triangles represent temporary stations deployed in the Weiyuan area. Yellow stars and green diamonds denote preliminary locations of the M_L 5.4 (W1), M_L 4.3 (W2), M_L 5.2 earthquake (W3), and catalog locations of the M_L 3.8 (R1) and M_L 2.5 (R2) reference earthquake. The red arrows show orientation of the local maximum principal stress from the image well logging analysis (Chen, Meng, et al., 2018).

Demonstration Area in the Sichuan Basin, China. These earthquakes are probably induced and have attracted extensive attention (e.g., Lei et al., 2017, 2019). In the Changning shale gas area, the background seismicity is relatively low, and only a few M > 5 earthquakes have been recorded before 2017 (Lei et al., 2019). However, induced earthquakes with M > 5 occur every year during the past 3 years. On 16 December 2018, an M5.7 earthquake struck Xingwen County in the Changning area. Eighteen days later, an M5.3 earthquake occurred 8 km to the west of the Xingwen earthquake. These events caused substantial casualties and property damage. Through a systematic analysis of source parameters, spatiotemporal correlation between the earthquake and hydraulic fracturing, seismicity, as well as overpressure for fault activation, Lei et al. (2019) concluded that the two earthquakes are induced by shale gas hydraulic fracturing at different well pads. The M5.7 Xingwen event is a typical strike-slip-dominated event, and the mechanism of the M5.3 event shows that both strike-slip and reverse components are almost equally important (Lei et al., 2019).

Earthquakes in the Weiyuan area provide another opportunity to investigate possible links between the seismicity and hydraulic fracturing of shale gas production in a region with compressional stress. In this area, no earthquake with M > 5.0 occurred before the shale gas production which started in 2014, according to the catalog from National Earthquake Data Center (NEDC) of China. However, three earthquakes with M > 4.0 occurred in the Weiyuan area since September 2019 (Figure 1). These three earthquakes killed one person and caused substantial property damages. According to the preliminary report of China Earthquake Network Center (CENC), these earthquakes, referred to as the Weiyuan earthquakes in this paper, are the M_L 5.4 earthquake (W1) at 22:42:14 UTC on 7 September 2019, the M_L 4.3 earthquake (W2) about 4 hr later, and the M_L 5.2 earthquake (W3) at 00:14:06 UTC on 18 December 2019. Depths of these earthquakes from the catalog are reported as 10, 7, and 14 km, respectively, but the depth accuracy has not been assessed yet (Table 1).

Hypocenter locations in the CENC catalog are routinely determined from P and/or S arrival times. The accuracy of the locations is mainly affected by station distribution, three-dimensional (3-D) heterogeneities of the velocity models, and uncertainties of the picked arrival times. For horizontal locations, the accuracy can reach 5 km if at least one station within 30 km (Bondár et al., 2004). Focal depth determined from P and S arrival times is reliable when the minimum epicenter distance is less than 1.4 times of the focal depth (Mori, 1991). Induced earthquakes usually have depths at about 2–5 km, which requires a station spacing of about 10 km to determine the depths using phase arrival times. In the Weiyuan area, the permanent seismic network can hardly meet this requirement, which has been improved as new stations being installed in this area after the M4.9 Rongxian earthquake on 25 February 2019.

Table 1
Source Parameters of Earthquakes in This Study, NP = Nodal Plane

| Event ID	Relocation Lon/Lat (deg)	Focal mechanism strike/dip/rake (deg) NP1	Focal mechanism strike/dip/rake (deg) NP2	Magnitude M_L	Magnitude Mw	Depth (km) Catalog	Depth (km) CAP
R1	104.823/29.537	185/69/84	21/22/105	3.8	3.42	12.0	2.5
R2	104.577/29.507	189/61/80	29/31/107	2.5	2.40	2.0	2.4
W1	104.812/29.602	201/68/75	57/26/123	5.4	4.97	10.0	2.9
W2	104.490/29.507	191/37/85	17/53/94	4.3	4.07	7.0	2.0
W3	104.844/29.642	205/64/80	47/28/110	5.2	4.78	14.0	2.9

In this paper, we used regional broadband seismic data to obtain focal mechanisms and centroid depths of the Weiyuan earthquakes with the cut-and-paste (CAP) method (Zhu & Helmberger, 1996). We first determined locations and focal mechanisms of two reference earthquakes recorded by a temporary dense seismic network. We then inverted the source parameters of the Weiyuan earthquakes and relocated their epicenters relative to the reference earthquakes. We also retrieved rupture directivities of W1 and W3 using a forward modeling technique to discriminate the actual fault plane from the auxiliary plane. In section 4, we analyzed links between the Weiyuan earthquakes and shale gas production. We also discussed possible triggering of W3 through analyses of rupture directivity and Coulomb stress changes of W1.

2. Geological Setting, Seismic Data, and Methods

The Weiyuan shale gas block is located in the southern part of the stable Sichuan Basin with a consolidated sedimentary layer of 4–6 km (Wang et al., 2016). The Weiyuan area lies in the southeast slope of the Leshan-Longnüsi paleo-uplift and the west side of the Early Cambrian "Mianyang-Changning" intracratonic sag, which is a large dome anticline (Liang et al., 2019). Rich and high-quality shale gas reservoirs have been found in the Upper Ordovician Wufeng Formation (O_3w)-Lower Silurian Longmaxi Formation (S_1l) in the Weiyuan area. The distribution of shale gas reservoir burial depth is in the range of 1.2–3.5 km (Liu & Wang, 2016). According to the image well logging analysis, multiscale natural fractures exit in the Weiyuan area, where the orientation of the local maximum principal stress is roughly N90°E (Chen, Meng, et al., 2018). The maximum principal stress axis estimated from earthquake focal mechanisms is almost horizontal with an azimuth of 106° (Lei et al., 2020).

In order to explore shallow velocity structures and monitor induced seismicity in the Weiyuan area, we deployed a temporary dense seismic array from November 2015 to November 2016 (Figure 1). The array consists of 50 Guralp CMG-40T seismographs with an average spacing of about 5 km. During summer of 2016, many of the stations stopped recording because of power surge from thunders and prolonged immersion during the rainy season. Zeng et al. (2020) extracted fundamental mode Rayleigh wave empirical Green's functions in the period band of 2–6 s from ambient seismic noises recorded by the array. Phase-velocity dispersion curves were measured to image 3-D shallow shear-velocity structures within 5 km of this area. Based on the 3-D structures, we construct an average 1-D velocity model for the upper crust (Figure 2a), which serves as the reference model for relocation and focal mechanism inversion of the reference earthquakes. In this model, the P velocities are calculated using a Vp/Vs ratio of 1.73 and 1.90 for the first and second layer, respectively, to fit the observed P wave arrival times. The large Vp/Vs ratio of the second layer is less reliable and mainly caused by underestimation of the S velocity from ambient noise tomography (Zeng et al., 2020). The P and S velocities below 10 km are identical to those in CRUST1.0 (Laske et al., 2013). Another velocity model obtained from passive and active seismic data for the Sichuan Basin (Figure 2b) is used for determining focal mechanisms and centroid depths of the Weiyuan earthquakes through waveform modeling (Zhao et al., 1997).

During this observational period, the array has recorded more than 800 earthquakes with $M_L > 1$ according to the catalog of NEDC. An M_L 3.8 earthquake (R1) occurred on 27 July 2016 near the preliminary report locations of W1 and W3, and an M_L 2.5 earthquake (R2) on 28 November 2015 lies close to the preliminary report location of W2 (Figure 1 and Table 1). Figure 3a displays an example of vertical-component waveforms from the M_L 2.5 earthquake, which show clear P, S, and surface waves with apparent velocities
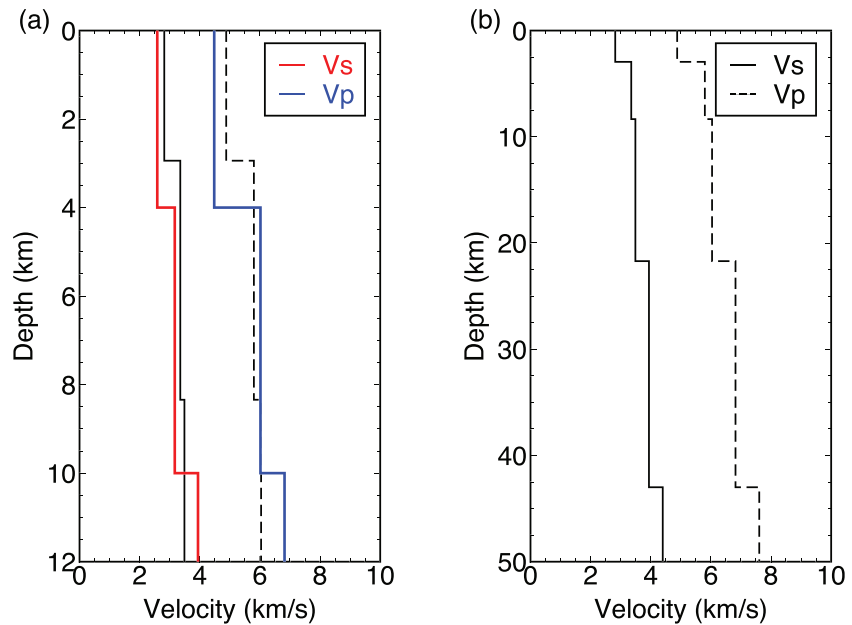
Figure 2. (a) *P* (blue) and *S* (red) velocity models for the Weiyuan area, modified from Zeng et al. (2020). The *Vp/Vs* ratio for the first and second layer are 1.73 and 1.90, respectively. The solid and dashed black lines are *P* and *S* velocities of the Sichuan Basin (Zhao et al., 1997), shown in (b).
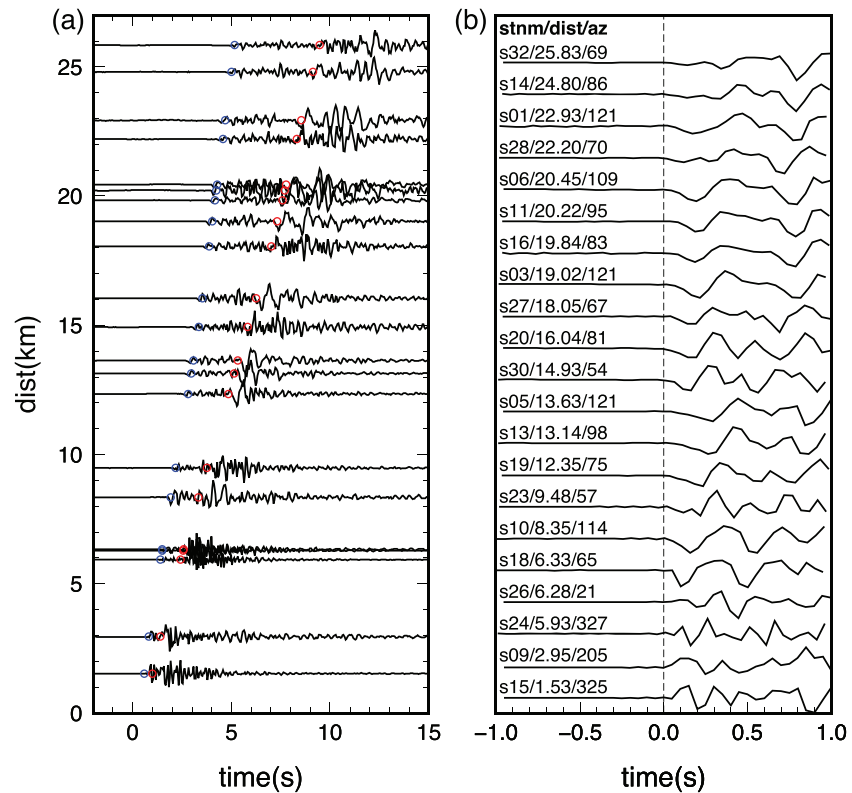
Figure 3. Vertical-component displacement waveforms of the M_L 2.5 event (R2) with clear *P* wave onset. (a) The blue and red circles mark the theoretical arrival times of *P* and *S* waves, respectively, for the Weiyuan velocity model shown in Figure 2a. (b) The *P* wave onset of the M_L 2.5 event, aligned with the picked *P* arrivals. The texts and numbers above each waveform show the station name, the epicenter distance in kilometers and azimuth in degrees. Each waveform is normalized to its maximum amplitude.

around 5.06, 2.95, and 2.55 km/s, respectively. The sharp *P* wave onsets enable precise measurements of the first arrivals (Figure 3b), which can be used to get accurate location of earthquakes.

We choose R1 and R2 as reference events to relocate the Weiyuan earthquakes. If the distance between an earthquake and the reference event is small compared to their epicenter distances and the length scale of the structure heterogeneity, the ray paths between these two events to a common station are almost identical. In this case, their differential travel times observed at the common station can be mainly attributed to the spatial offset between the event pair (Chu et al., 2011; Waldhauser & Ellsworth, 2000). Here we will use surface wave differential travel times for relocation. With relatively stronger amplitudes and lower frequencies than body waves, surface waves have higher signal-to-noise ratios (SNRs) and longer wave lengths, therefore are less affected by velocity heterogeneity near the source region. Another advantage of the surface waves is that they have lower apparent velocity, which yields higher spatial resolution of event locations than the body waves (Zhan et al., 2011).

When the distance between two events are small enough, the differential travel time Δt of surface waves can be approximated as a trigonometric function of the station azimuth θ,

$$\Delta t = \Delta t_0(O, h) + \frac{\Delta r}{v} \cos(\theta - \theta_0), \tag{1}$$

where Δt_0 is a constant related to origin times and depths of the two events and v represents the apparent surface wave velocity near the source region. We can fit the differential travel time curve to determine Δr and θ_0, which are distance and azimuth of the earthquake relative to the reference.

Depths and focal mechanisms of the Weiyuan earthquakes can be obtained through the CAP waveform inversion method, which has been widely used in the study of induced earthquakes in the Sichuan Basin (Lei et al., 2017, 2019). The CAP method uses a grid search approach in the source parameter domain (strike, dip, rake, and centroid depth) for best-fitting regional broadband waveforms (Chu & Helmberger, 2013; Zhu & Ben-Zion, 2013; Zhu & Helmberger, 1996). The synthetic waveforms are a summation of Green's functions calculated from a 1-D velocity model using the frequency-wave number integration method (Zhu & Rivera, 2002). The observed and synthetic waveforms are divided into *Pnl* and surface wave segments, and each segment is filtered at different frequency band and allowed an independent time shift to correct travel-time errors from inaccurate source parameters and deviation from true heterogeneous velocity structures.

3. Source Parameters of the Weiyuan Earthquakes

Since the reference earthquakes are small and the waveforms have relatively low SNR at regional distances, we use the data recorded by the temporary dense array to determine their source parameters. We first remove the mean value, linear trend, and instrument response from the waveform data and then rotate the three-component velocity seismograms to radial, tangential, and vertical components in the RTZ coordinates. Most of the epicenter distance of these two earthquakes are less than 50 km; the body and surface waves can hardly be separated in the low frequency band. Thus, we treat the body and surfaces waves as a whole to invert for the focal mechanisms, similar to the method in Herrmann et al. (2011). Seismic waveforms are filtered at a frequency band of 0.3–0.6 Hz for inversion of reference earthquakes. The grid search steps are 5° for strike, dip, and rake angles and 0.5 km for centroid depth. Focal mechanism inversion results indicate that optimal centroid depths of R1 and R2 are 2.5 and 2.4 km, respectively, and both earthquakes have thrusting focal mechanisms (Table 1). An example of the waveform fitting for R2 is displayed in Figure 4, and waveform fitting for R1 can be found in Figure S1 in the supporting information.

R1 is also recorded by some nearby permanent stations, which can be used to invert for its focal mechanism. We download broadband waveform data of R1 from the Data Management Center of China National Seismic Network (Zheng et al., 2010). Data with low SNR are rejected after visual inspection. We select 14 stations with good azimuth coverage and clear waveforms to determine its focal mechanism and centroid depth. The broadband waveforms are cut into 35 s segments for body waves and 70 s segments for surface waves and then filtered with frequency bands of 0.05–0.2 and 0.02–0.1 Hz, respectively. The parameters in the grid search are identical to those for the temporary array. The focal mechanism and centroid depth
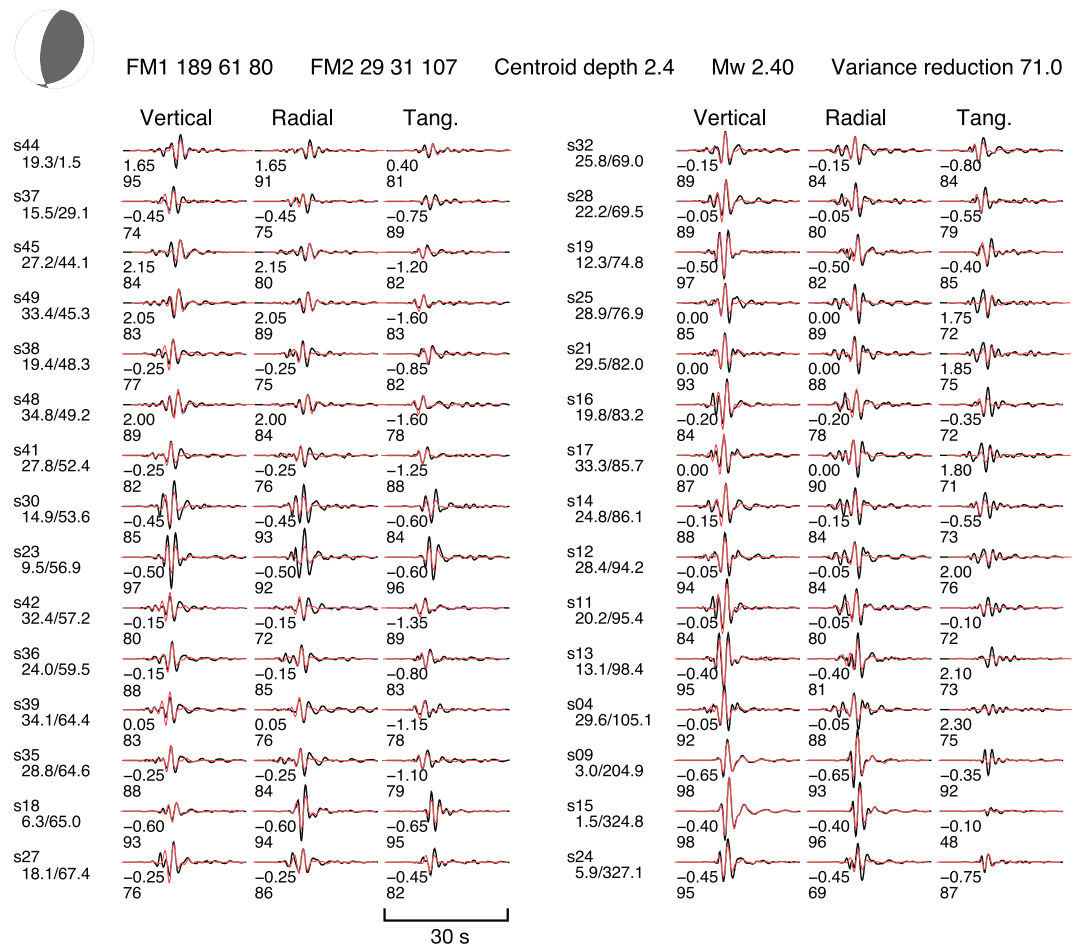
Figure 4. Focal mechanism inversion for R2 through data from the temporary dense seismic array. The black and red are observed and synthetic waveforms. The texts before each row are station name, distance in kilometers, and azimuth in degrees. The numbers below each segment show the timing shifts and the cross-correlation coefficients. Positive time shifts indicate that the output synthetics need to be shifted back, that is, late observed arrivals.

are strike/dip/rake = 191°/61°/90° and 3.0 km, respectively, similar to those obtained from the temporary array data (Figure S2), which justifies reliable inversions for the focal mechanisms of R1 and R2 using the temporary array data.

The Weiyuan earthquakes are large enough to be well recorded by regional permanent stations within 300 km. We deploy the same inversion strategy and parameters as the inversion for R1 using permanent station data, except the frequency band of 0.05–0.2 Hz for the body waves. The best-fitting focal mechanism and waveform fitting for W1 are shown in Figure 5, whereas the inversion results and waveform fittings for W2 and W3 are shown in Figures S3 and S4, respectively. W1–W3 all have thrusting mechanisms with optimal centroid depths at 2.9, 2.0, and 2.9 km, respectively (Figure 6).

We then carry out a bootstrapping approach (Chu & Helmberger, 2013; Efron & Tibshirani, 1986; Sheng et al., 2020) to analyze uncertainty of the focal mechanism solutions for W1. Here we randomly select a set of 34 broadband waveforms from the 34 stations in Figure 5 to invert for the focal mechanism, which allows multiple sampling of each station with different weights. We repeat the inversion to obtain 1,000 focal mechanisms. Histograms of the strike, dip, and rake of the 1,000 focal mechanisms show a highly concentrated distribution around those from all stations (Figure S5), indicating a reliable focal mechanism.

As centroid depth is a key parameter to discriminate whether an earthquake is induced or not, we use other two 1-D velocity models to invert centroid depths of the Weiyuan earthquakes. The first model is an average
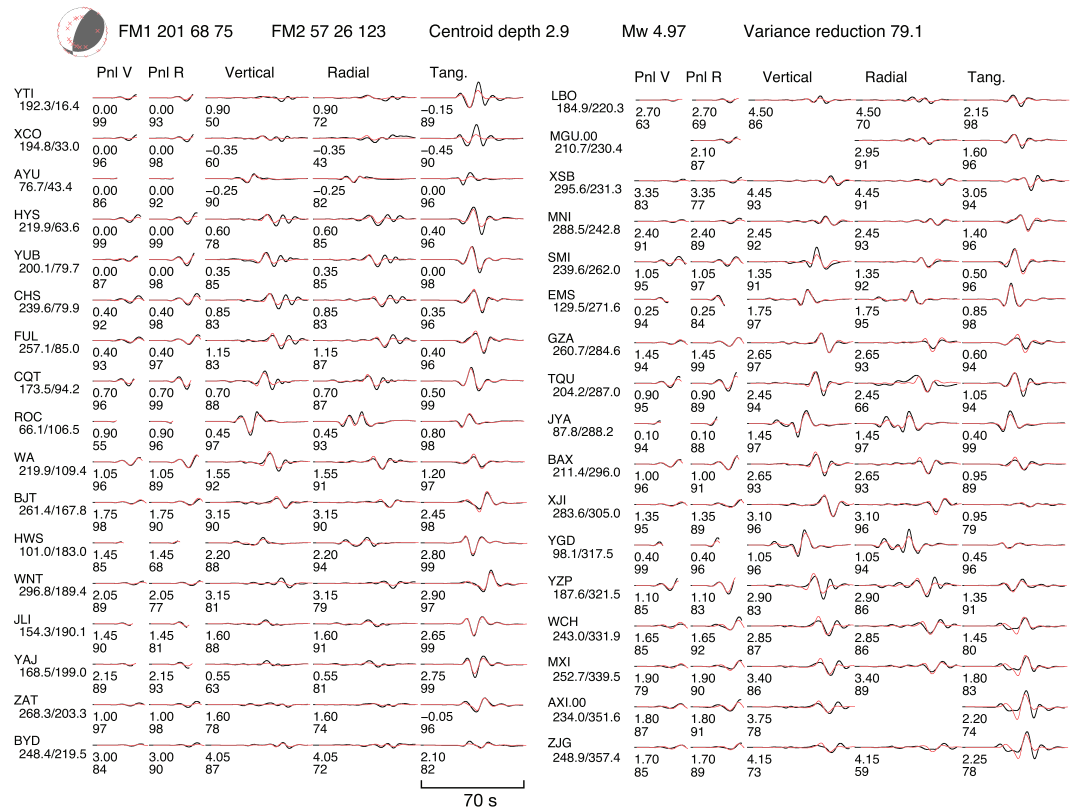
Figure 5. Focal mechanism inversion for W1 through data from the permanent stations. The waveforms data (black) are cut into *Pnl* and surface wave sections and fitted by the synthetics (red) with different time shifts. Text and symbols are the same as those in Figure 4.
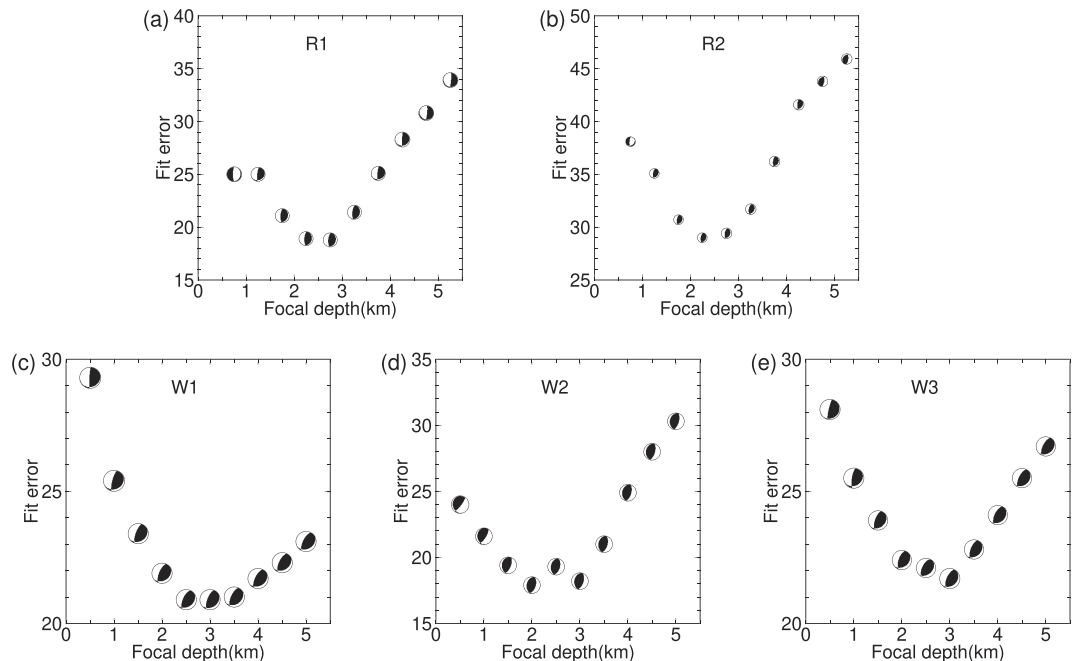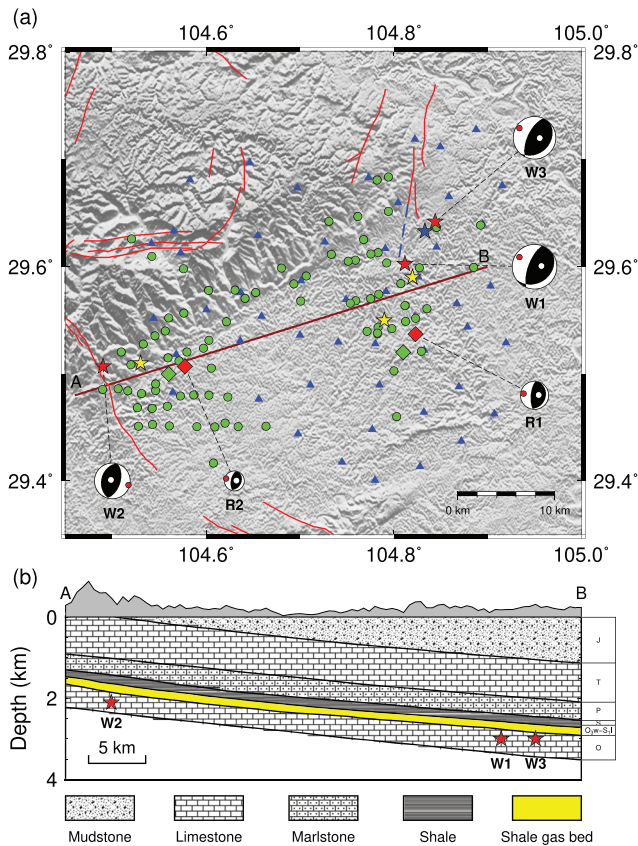

Figure 6. Depth resolution of misfit versus focal depth for the reference (a and b) and Weiyuan (c–e) earthquakes.

Figure 7. (a) Relocation of the reference earthquakes and the Weiyuan earthquakes. The symbols are temporary seismic stations (blue triangles), official catalog locations of the reference earthquakes (green diamonds), the relocated reference earthquakes (red diamonds), preliminary report locations of the Weiyuan earthquakes (yellow stars), the relocated Weiyuan earthquakes (red stars), relative location of W3 to W1 (blue star), and injection wells in the Weiyuan area (green circles) identified during the seismometer deployment and from Google Earth satellite images. Red and white circles on each focal mechanism indicate the P and T axis, respectively. Red lines denote local faults from Liang et al. (2019). (b) Geological setting along the AB profile in the Weiyuan shale gas field, modified from Zou et al. (2020). Stars depict centroid depths of the Weiyuan earthquakes.

velocity model beneath the Sichuan Basin derived from surface wave dispersion, which is primarily a S velocity model (Shen et al., 2016). The second model is for the southern Sichuan Basin derived from P and S wave arrival times (Yi et al., 2019). The best centroid depths obtained from the model of Shen et al. (2016) are 3.2, 2.6, and 2.9 km for W1–W3, respectively, whereas the model of Yi et al. (2019) renders centroid depths of 3.4, 2.1, and 2.5 km for W1–W3, respectively (Figure S6). Different velocity models all yield shallow depths for the Weiyuan earthquakes. We also calculate full moment tensors for the Weiyuan earthquakes using different velocity models, which display small nondouble-couple components (Figure S7).

Table 1 lists detailed source parameters for the references and the Weiyuan earthquakes. It is clear that focal mechanisms and centroid depths of W1 and W3 are similar to those of R1, which is helpful for reliable measurements of differential arrival times and precise relocations of these two earthquakes. On the other hand, the focal mechanism of W2 is similar to that of R2, but the difference of their dipping angle is greater than 25° (Table 1). This large difference in focal mechanism may affect the accuracy of W2 relocation. However, Zeng et al. (2015) assessed the effects of earthquake focal mechanisms on Rayleigh wave group arrival times and found that the effect will be smaller for shallower earthquakes. Since both R2 and W2 are less than 3.0 km, the effect of the focal mechanisms would be negligible.

We manually pick the P wave onsets (Figure 3b) and then determine hypocenters of R1 and R2 using the hypo2000 method (Klein, 2002). The 1-D velocity model used here is the average structure from the ambient seismic tomography (Figure 2a). Figure 7a displays the relocated R1 and R2, which are about 2.0 km to the northeast of the catalog locations. The horizontal uncertainties of R1 and R2 are 0.6 and 0.25 km, respectively. R1 has a larger uncertainty than R2 because R1 occurred in the rainy season with fewer available stations. The depth of R1 is 3.3 km with an uncertainty of about 1.0 km, whereas R2 has a depth of 2.7 km with an uncertainty of 0.75 km. The hypo2000 relocation results indicate the R1 event is deeper than the R2 event, which is consistent with those from the CAP inversion. As the rupture length of an M ~ 3 earthquake is about 0.3 km and the wavelength is more than 3 km for 0.4–0.8 Hz surface waves, we treat hypocenters of the reference earthquakes as their centroids in this paper.

We then relocate the Weiyuan earthquakes using the refined R1 and R2 locations. Differential surface wave travel times are measured from cross correlations of high-quality Rayleigh waves recorded by the permanent stations in the frequency range of 0.4–0.8 Hz. At this frequency band, the Rayleigh wave phase velocity is about 2.45 km/s based on the dispersion curve (Zeng et al., 2020). The differential travel times of W1 with respect to R1 are shown in Figure 8a. We fit the differential travel times using a least square method, yielding $\Delta r = 7.2 \pm 0.56$ km and $\theta_0 = 170° \pm 4.9°$, which indicates that W1 lies in the direction of 350° to R1 with a distance of about 7.2 km (Figure 7a). The 95% confidence bounds of the curve fitting for the differential travel times are shown in Figure 8, based on which the uncertainties of θ_0 and Δr can be calculated using the phase velocity. With the same approach, we obtain the differential travel time of W2 and W3 with respect to R2 and R1 (Figures 8b and 8c), respectively, to relocate centroids of W2 and W3, as displayed in Figure 7a.

The reference earthquakes are too small to generate low-frequency surface waves. Here we try to filter the surface waves in a lower frequency band of 0.167–0.4 Hz, with Rayleigh wave phase velocity at about 2.53 km/s, to verify our location results. In this frequency band, the epicenters of W1 and W3 are almost identical to those in the frequency band of 0.4–0.8 Hz, with an error of less than 0.1 km (Figures 8a and 8c). We
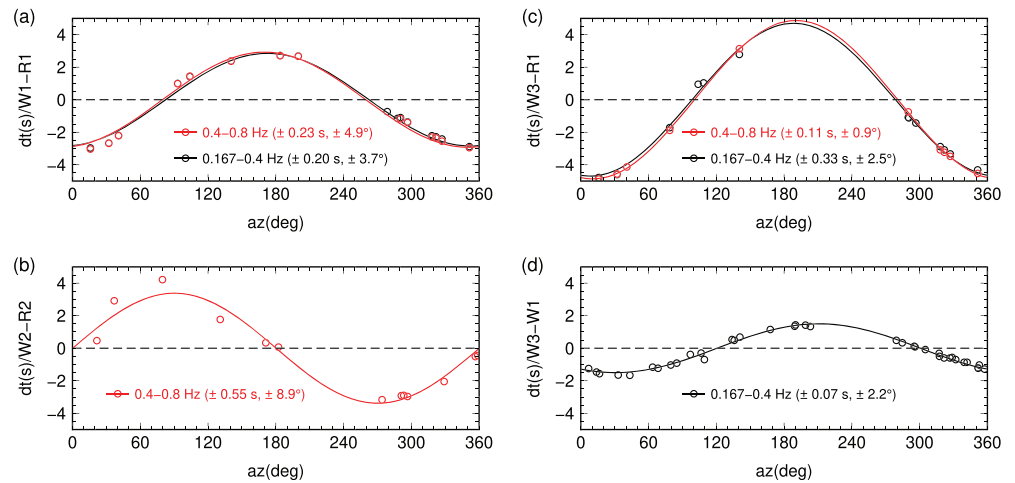
Figure 8. Surface wave differential travel times for event pairs of W1-R1 (a), W2-R2 (b), W3-R1 (c), and W3-W1 (d) as a function of station azimuth. The red and black dots display observed differential travel times in the frequency band of 0.4–0.8 and 0.167–0.4 Hz, respectively. The red and black lines are the best-fitting sinusoidal functions at those frequency bands and the text in brackets indicates the 95% confidence bounds of the amplitude and phase of the curve fitting.

do not determine the W2 centroid location because R2 has no clear surface waves in the frequency band of 0.167–0.4 Hz. We can also use W1 as a reference to relocate W3 since they have similar source parameters. The W3 is about 2 km closer to W1 than that determined using R1 (Figures 7 and 8d), which might be caused by rupture directivity of these two earthquakes.

Rupture directivity is an important earthquake source parameter to describe its kinetic processes, which will cause an azimuthal variation of source time durations. Usually, the maximum duration appears opposite to the rupture direction, and the minimum is in the rupture direction, related to the Doppler effect of seismic waves. Therefore, earthquake rupture directivity can be used to discriminate the actual fault plane from the auxiliary plane. Since W2 is an M ~ 4 earthquake, we first apply the method in Tan and Helmberger (2010) to obtain the rupture directivity of W1 and W3 through azimuthal variation of their source durations. Here we use waveforms of R1 as empirical Green's functions to estimate the durations of source time function (STF) of W1 for 10 stations. Specifically, we filter the R1 and W1 waveforms in a frequency band of 0.125–2 Hz. The upper frequency limit is lower than the corner frequency of R1 and higher than that of W1, so that R1 can be regarded as a point source and W1 shows directivity effect. We construct 10 trapezoidal STFs with different durations and a rise time of $\frac{1}{3}$ and convolve with the vertical component waveforms of R1, to generate synthetic waveforms. We then cut *P* waves of R1 and W1 with 1 s before and 6 s after the first arrivals and find the STF with the best waveform fitting which has the largest cross-correlation coefficient (Figure 9).

For earthquakes rupturing along a dipping fault plane, the observed STFs depend on the fault geometry, take-off angle, and azimuth of the station (Park & Ishii, 2015). Warren and Silver (2006) and Abercrombie et al. (2017) considered this STF feature and analyzed rupture directivities for deep earthquakes with teleseismic waveforms and shallow events with local data, respectively. However, W1 in this study is a shallow earthquake and the waveforms at regional distances are complicated due to a mixture of upgoing and downgoing waves. We cannot adopt the method presented in those two studies to infer the up-dip or down-dip directivity. Fortunately, the observed azimuthal variation of source durations can still be used to infer the horizontal directivity when the take-off angles are similar (Park & Ishii, 2015). We then choose stations within an epicenter distance range of 168–200 km (Figure 9) and also infer a horizontal rupturing to the northeast.

Since W1 has two nodal planes striking at 57° and 201°, respectively (Table 1), the earthquake will rupture in the direction of either 57° (237°) or 201° (21°). Our STF result suggests that the duration is smallest in the azimuth of ~23° (Figure 9b), indicating that the fault plane of W1 is 201°/68°/75° and its rupture directivity is from southwest to northeast. The fault plane and rupture directivity of W3 are similar to those of W1
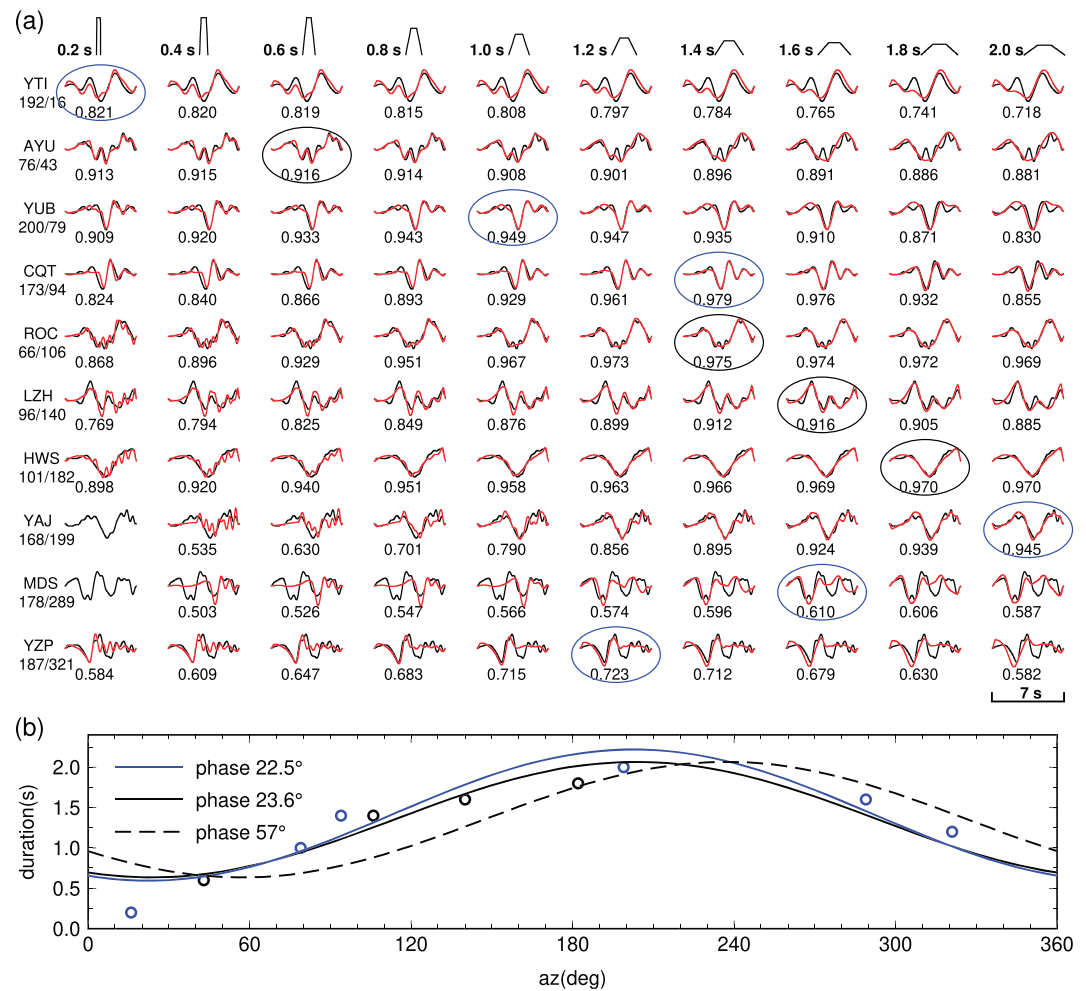
Figure 9. Duration of source time functions (STFs) of W1. (a) Waveform fits for the observed *P* wave vertical displacement of W1 (black) and synthetics (red). Each synthetic waveform is constructed from convolution of the EGF from R1 and STF on the top. The STFs are trapezoidal function with a $\frac{1}{3}$ rise time. Ovals mark the best-fitting STFs with the highest cross-correlation coefficient, which is below each segment. The texts before each row are station name, distance in kilometers, and azimuth in degrees. (b) Best-fitting sinusoidal function between the station azimuth and duration of the STF for W1, suggesting a rupture directivity from SW to NE. Blue ovals, circles, and solid line represent the results from those stations with similar take-off angles. Black solid line represents the results for all 10 stations. The dashed line is the duration of the STF corresponding to a rupture direction of 57° (i.e., NP2 in Table 1).

(Figure 10). The consistent rupture direction of W1 and W3 may provide important information for understanding the mechanism of induced earthquakes and material properties across the fault (Rubin & Gillard, 2000). It should be noted that the fault planes in this study are inferred solely from the rupture directivity, and we cannot completely rule out the possibility that the Weiyuan earthquakes rupture along the other fault plane.

4. Discussion

Shale gas resources in the Sichuan Basin are mainly distributed in the Upper Ordovician Wufeng Formation (O_3w)-Lower Silurian Longmaxi Formation (S_1l). Particularly, the Longmaxi Formation is the "sweet spot" for shale gas production in the Weiyuan area, based on drilling and pilot production data, as well as the geological, geochemical, geophysical, and rock mechanics observations (Liu & Wang, 2016). The bottom boundary of the Upper Ordovician Wufeng Formation varies from nearly 2.0 km around R2 to nearly 3.0 km near R1 (Figure 7b). Injection wells in this area are also at a depth of 2–4 km (Lei et al., 2017),
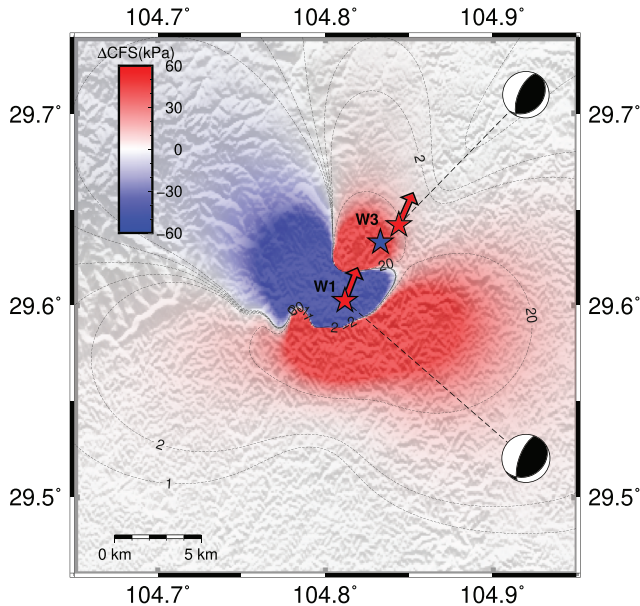
Figure 10. Rupture directivity of W1 and W3 (red arrow) and the Coulomb stress changes caused by W1. The red stars are relative locations of W1 and W3 with respect to R1, whereas the blue star denotes the W3 centroid relocated with respect to W1.

which agree with the best centroid depths of 3 km for R1, W1, and W3 and 2 km for R2 and W2, respectively. Therefore, shallow depth distribution of the Weiyuan earthquakes suggests that these events are likely related to hydraulic fracturing during the shale gas production.

The distance between the earthquake centroids and injection wells may be an indicator that the Weiyuan earthquakes are induced. Although the industrial data and location of the injection wells are not open to the public, we can still identify some injection platforms during the seismograph deployment and through satellite images (Figure 7a). The injection wells are highly concentrated in the east and west of the Weiyuan area, where the earthquakes occur. All earthquakes are within 2 km to injection wells, which suggest that the earthquakes are very likely to be induced by injection activities. Similar to the 2018 Xingwen earthquake, W1 and W3 are probably nucleated within a zone of elevated pore pressure near injection wells and rupture unidirectionally to the northeast beyond the zone (Lei et al., 2020).

In this study, the centroid distance between W1 and W3 is 5–7 km, the static triggering caused by permanent stress change from fault displacement of W1 may affect the occurrence of W3. We calculate the static Coulomb stress change (ΔCFS) caused by fault slip of W1 for the receiving fault of W3, using the method of Wang et al. (2006),

$$\Delta \text{CFS} = \Delta\tau + \mu(\Delta\sigma + \Delta P) = \Delta\tau + \mu'\Delta\sigma, \qquad (2)$$

where $\Delta\tau$ and $\Delta\sigma$ are changes in the shear stress and normal stress, respectively, for a given fault geometry and slip direction, ΔP is the change of pore fluid pressure, and μ is the friction coefficient. $\mu' = \mu(1 - \beta)$ is the effective coefficient of friction. We take $\mu = 0.6$ and $\beta = 0.47$ according to Lei et al. (2019) and Sumy et al. (2014). Rupture dimension and average fault slip are estimated from their empirical relationships with earthquake magnitude (Wells & Coppersmith, 1994). Detailed calculation steps and strategies can be found in Cheng et al. (2016) and Pang et al. (2020). The result shows that W3 is located in a positive area with ΔCFS exceeding 20 kPa (Figure 10), which is larger than a typical threshold of 10 kPa to trigger W3 (Brodsky & Prejean, 2005; Cochran et al., 2004). However, W3 occurred about 4 months after W1. It can be noted that there is an injection well near W3 (Figure 7a). In addition, hydraulic fracturing operations can result in much greater CFS by poroelastic effect (Lei et al., 2017) at such a distance of W3 from the neatest injection well. The long time lapse and a very close injection well indicate that W3 is more likely induced by hydraulic fracturing than triggered by static stress change of W1. In our study, the change of pore fluid pressure and friction coefficient is highly variable and will yield some uncertainties to our estimation of ΔCFS. Moreover, the industrial data is unavailable, including injected water volume and rate after W1. In the future, we will try to combine industrial data, source parameters of W1 aftershocks and geodetic measurements to investigate possible mechanisms of W3. It is also necessary to simulate fluid migration in the compressional environment to clarify the physical processes with the injected water data.

Some unconventional hydraulic fracturing has produced high level of seismicity, whereas the others are lack of induced seismicity, which indicates that the relationship between hydraulic fracturing and induced seismicity is likely to be influenced by the tectonic setting (Atkinson et al., 2020). In the Sichuan Basin, hydraulic fracturing activities have been carried out in four regions, that is, Jiaoshiba, Changning, Weiyuan, and Weixi. The Changning and the Weiyuan areas have experienced earthquakes with $M_L > 5.0$. Since 2016, six earthquakes with M_L 4.0–4.9 occurred in Weixi. The Jiaoshiba area has higher density of faults, similar to the Changning and Weixi sites, but have the lowest level of induced seismicity. This could be explained by the stress pattern, under which the stress from hydraulic fracturing is insufficient to activate unfavorable faults (Lei et al., 2019). In the Weiyuan area, the average orientation of the maximum principal horizontal stress is roughly N90°E derived from image well logging analysis (Figure 1a). The stress orientation is consistent to the P axis of the earthquake focal mechanism in this area (Figure 7), indicating faults are optimally

oriented with respect to the regional stress field and will be readily reactivated. On the other hand, Lei et al. (2020) obtained the stress shape ratio from earthquake focal mechanisms as $\phi = \dfrac{\sigma_2 - \sigma_3}{\sigma_1 - \sigma_3} = 0.91 \pm 0.08$ and concluded that reverse faults of any strike direction could be easily reactivated in such a stress regime.

5. Conclusion

In summary, we obtain high-precision source parameters of two small earthquakes recorded by a dense seismic network and take them as references to determine centroid location of three moderate-size earthquakes in the Weiyuan area. All these earthquakes have thrusting focal mechanisms with a centroid depth no larger than 3.0 km and are located within 2 km to water injection wells. We also resolve rupture directivity of the $M_L 5.4$ and $M_L 5.2$ earthquakes by using waveforms of the nearby reference earthquake as empirical Green's functions, and both earthquakes rupture to NE. The $M_L 5.2$ event is located in an area with positive Coulomb stress change. The long time lapse of the $M_L 5.2$ earthquake and the existence of a near injection well suggest that it is more likely induced by hydraulic fracturing than triggered statically by the $M_L 5.4$ earthquake.

Data Availability Statement

Waveform data for the reference earthquakes can be downloaded at Mendeley Data (https://doi.org/10.17632/jj2s4c5y8m). The earthquake catalog is provided by National Earthquake Data Center of China (http://data.earthquake.cn).

References

Abercrombie, R. E., Poli, P., & Bannister, S. (2017). Earthquake directivity, orientation, and stress drop within the subducting plate at the Hikurangi margin, New Zealand. *Journal of Geophysical Research: Solid Earth*, *122*, 10,176–10,188. https://doi.org/10.1002/2017JB014935

Atkinson, G. M., Eaton, D. W., & Igonin, N. (2020). Developments in understanding seismicity triggered by hydraulic fracturing. *Nature Reviews Earth & Environment*, *1*(5), 264–277. https://doi.org/10.1038/s43017-020-0049-7

Bondár, I., Myers, S. C., Engdahl, E. R., & Bergman, E. A. (2004). Epicentre accuracy based on seismic network criteria. *Geophysical Journal International*, *156*(3), 483–496. https://doi.org/10.1111/j.1365-246X.2004.02070.x

Brantut, N., & Platt, J. D. (2017). Dynamic weakening and the depth dependence of earthquake faulting. In *Fault Zone Dynamic Processes: Evolution of Fault Properties During Seismic Rupture*, *Geophysical Monograph Series* (Vol. 227, pp. 171–194). Washington, D. C: American Geophysical Union.

Brodsky, E. E., & Prejean, S. G. (2005). New constraints on mechanisms of remotely triggered seismicity at Long Valley Caldera. *Journal of Geophysical Research*, *110*, B04302. https://doi.org/10.1029/2004JB003211

Chen, H., Meng, X., Niu, F., Tang, Y., Yin, C., & Wu, F. (2018). Microseismic monitoring of stimulating shale gas reservoir in SW China: 2. Spatial clustering controlled by the preexisting faults and fractures. *Journal of Geophysical Research: Solid Earth*, *123*, 1659–1672. https://doi.org/10.1002/2017JB014491

Chen, X., Haffener, J., Goebel, T. H. W., Meng, X., Peng, Z., & Chang, J. C. (2018). Temporal correlation between seismic moment and injection volume for an induced earthquake sequence in central Oklahoma. *Journal of Geophysical Research: Solid Earth*, *123*, 3047–3064. https://doi.org/10.1002/2017JB014694

Cheng, H., Zhang, H., & Shi, Y. (2016). High-resolution numerical analysis of the triggering mechanism of M_L 5.7 Aswan reservoir earthquake through fully coupled poroelastic finite element modeling. *Pure and Applied Geophysics*, *173*(5), 1593–1605.

Chu, R., & Helmberger, D. V. (2013). Source parameters of the shallow 2012 Brawley earthquake, Imperial Valley. *Bulletin of the Seismological Society of America*, *103*(2A), 1141–1147. https://doi.org/10.1785/0120120324

Chu, R., Wei, S., Helmberger, D. V., Zhan, Z., Zhu, L., & Kanamori, H. (2011). Initiation of the great Mw 9.0 Tohoku-Oki earthquake. *Earth and Planetary Science Letters*, *308*, 277–283.

Cochran, E. S., Vidale, J. E., & Tanaka, S. (2004). Earth tides can trigger shallow thrust fault earthquakes. *Science*, *306*(5699), 1164–1166. https://doi.org/10.1126/science.1103961

Davis, S. D., & Frohlich, C. (1993). Did (or will) fluid injection cause earthquakes? Criteria for a rational assessment. *Seismological Research Letters*, *64*(3–4), 207–224. https://doi.org/10.1785/gssrl.64.3-4.207

Efron, B., & Tibshirani, R. (1986). Bootstrap methods for standard errors, confidence intervals, and other measures of statistical accuracy. *Statistical Science*, *1*(1), 54–75. https://doi.org/10.1214/ss/1177013815

Ellsworth, W. L. (2013). Injection-induced earthquakes. *Science*, *341*(6142), 1225942. https://doi.org/10.1126/science.1225942

Grigoli, F., Cesca, S., Rinaldi, A. P., Manconi, A., López-Comino, J. A., Clinton, J. F., et al. (2018). The November 2017 Mw 5.5 Pohang earthquake: A possible case of induced seismicity in South Korea. *Science*, *360*(6392), 1003–1006. https://doi.org/10.1126/science.aat2010

Herrmann, R. B., Benz, H., & Ammon, C. J. (2011). Monitoring the earthquake process in North America. *Bulletin of the Seismological Society of America*, *101*(6), 2609–2625. https://doi.org/10.1785/0120110095

Huang, Y., Wu, J., Zhang, T., & Zhang, D. (2008). Relocation of the M8.0 Wenchuan earthquake and its aftershock sequence. *Science China Earth Sciences*, *51*(12), 1703–1711.

Hubbard, J., & Shaw, J. (2009). Uplift of the Longmen Shan and Tibetan plateau, and the 2008 Wenchuan (M = 7.9) earthquake. *Nature*, *458*(7235), 194–197. https://doi.org/10.1038/nature07837

Keranen, K. M., & Weingarten, M. (2018). Induced seismicity. *Annual Review of Earth and Planetary Sciences*, *46*(1), 149–174. https://doi.org/10.1146/annurev-earth-082517-010054

Keranen, K. M., Weingarten, M., Abers, G. A., Bekins, B. A., & Ge, S. (2014). Sharp increase in central Oklahoma seismicity since 2008 induced by massive wastewater injection. *Science*, *345*(6195), 448–451. https://doi.org/10.1126/science.1255802

King, V. M., Block, L. V., Yeck, W. L., Wood, C. K., & Derouin, S. A. (2014). Geological structure of the Paradox Valley Region, Colorado, and relationship to seismicity induced by deep well injection. *Journal of Geophysical Research: Solid Earth*, *119*, 4955–4978. https://doi.org/10.1002/2013JB010651

Klein, F. W. (2002). User's guide to HYPOINVERSE2000, a Fortran program to solve for earthquake locations and magnitudes, U. S. Geol. Surv.

Laske, G., Masters, G., Ma, Z., & Pasyanos, M. (2013). Update on CRUST1.0—A 1-degree Global Model of Earth's Crust, Geophys. Res. Abstracts, 15, Abstract EGU2013–2658.

Lei, X., Huang, D., Su, J., Jiang, G., Wang, X., Wang, H., et al. (2017). Fault reactivation and earthquakes with magnitudes of up to Mw 4. 7 induced by shale-gas hydraulic fracturing in Sichuan basin, China. *Scientific Reports*, *7*(1), 7971.

Lei, X., Su, J., & Wang, Z. (2020). Growing seismicity in the Sichuan Basin and its association with industrial activities. *Science China Earth Sciences*. https://doi.org/10.1007/s11430-020-9646-x

Lei, X., Wang, Z., & Su, J. (2019). The December 2018 ML 5.7 and January 2019 ML 5.3 earthquakes in South Sichuan basin induced by shale gas hydraulic fracturing. *Seismological Research Letters*, *90*(3), 1099–1110.

Liang, X., Liu, S., Wang, S., Deng, B., Zhou, S., & Ma, W. (2019). Analysis of the oldest carbonate gas reservoir in China—New geological significance of the Dengying gas reservoir in the Weiyuan Structure, Sichuan Basin. *Journal of Earth Science*, *30*(2), 348–366. https://doi.org/10.1007/s12583-017-0962-y

Liu, J., & Zahradník, J. (2020). The 2019 MW 5.7 Changning earthquake, Sichuan Basin, China: A shallow doublet with different faulting styles. *Geophysical Research Letters*, *47*, e2019GL085408. https://doi.org/10.1029/2019GL085408

Liu, N., & Wang, G. (2016). Shale gas sweet spot identification and precise geo-steering drilling in Weiyuan block of Sichuan Basin, SW China. *Petroleum Exploration and Development*, *43*(6), 1067–1075. https://doi.org/10.1016/S1876-3804(16)30124-0

Luo, Y., Ni, S., Zeng, X., Xie, J., Chen, Y., & Long, F. (2011). The M5.0 Suining-Tongnan (China) earthquake of 31 January 2010: A destructive earthquake occurring in sedimentary cover. *Chinese Science Bulletin*, *56*, 521–525.

Marone, C., & Scholz, C. H. (1988). The depth of seismic faulting and the upper transition from stable to unstable slip regimes. *Geophysical Research Letters*, *15*(6), 621–624. https://doi.org/10.1029/GL015i006p00621

McNamara, D. E., Benz, H. M., Herrmann, R. B., Bergman, E. A., Earle, P., Holland, A., et al. (2015). Earthquake hypocenters and focal mechanisms in central Oklahoma reveal a complex system of reactivated subsurface strike-slip faulting. *Geophysical Research Letters*, *42*, 2742–2749. https://doi.org/10.1002/2014GL062730

Mori, J. (1991). Estimates of velocity structure and source depth using multiple *P* waves from aftershocks of the 1987 Elmore ranch and Superstition Hills, California, earthquakes. *Bulletin of the Seismological Society of America*, *81*(2), 508–523.

Pang, Y., Zhang, H., Cheng, H., Shi, Y., Fang, C., Luan, X., et al. (2020). The modulation of groundwater exploitation on crustal stress in the North China Plain, and its implications on seismicity. *Journal of Asian Earth Sciences*, *189*, 104141. https://doi.org/10.1016/j.jseaes.2019.104141

Park, S., & Ishii, M. (2015). Inversion for rupture properties based upon 3-D directivity effect and application to deep earthquakes in the Sea of Okhotsk region. *Geophysical Journal International*, *203*(2), 1011–1025. https://doi.org/10.1093/gji/ggv352

Qian, Y., Chen, X., Luo, H., Wei, S., Wang, T., Zhang, Z., & Luo, X. (2019). An extremely shallow Mw4.1 thrust earthquake in the eastern Sichuan Basin (China) likely triggered by unloading during infrastructure construction. *Geophysical Research Letters*, *46*, 13,775–13,784. https://doi.org/10.1029/2019GL085199

Rubin, A. M., & Gillard, D. (2000). Aftershock asymmetry/rupture directivity among central San Andreas fault microearthquakes. *Journal of Geophysical Research*, *105*(B8), 19,095–19,109. https://doi.org/10.1029/2000JB900129

Rubinstein, J. L., & Mahani, A. B. (2015). Myths and facts on waste-water injection, hydraulic fracturing, enhanced oil recovery, and induced seismicity. *Seismological Research Letters*, *86*(4), 1060–1067. https://doi.org/10.1785/0220150067

Schultz, R., Wang, R., Gu, Y. J., Haug, K., & Atkinson, G. (2017). A seismological overview of the induced earthquakes in the Duvernay play near Fox Creek, Alberta. *Journal of Geophysical Research: Solid Earth*, *122*, 492–505. https://doi.org/10.1002/2016JB013570

Shen, W., Ritzwoller, M. H., Kang, D., Kim, Y., Lin, F. C., Ning, J. Y., et al. (2016). A seismic reference model for the crust and uppermost mantle beneath China from surface wave dispersion. *Geophysical Journal International*, *206*(2), 954–979. https://doi.org/10.1093/gji/ggw175

Sheng, M., Chu, R., Wang, Y., & Wang, Q. (2020). Inversion of source mechanisms for single-force events using broadband waveforms. *Seismological Research Letters*, *91*(3), 1820–1830. https://doi.org/10.1785/0220190349

Sumy, D. F., Cochran, E. S., Keranen, K. M., Wei, M., & Abers, G. A. (2014). Observations of static Coulomb stress triggering of the November 2011 M5.7 Oklahoma earthquake sequence. *Journal of Geophysical Research: Solid Earth*, *119*, 1904–1923. https://doi.org/10.1002/2013JB010612

Sun, X., Yang, P., & Zhang, Z. (2017). A study of earthquakes induced by water injection in the Changning salt mine area, SW China. *Journal of Asian Earth Sciences*, *136*, 102–109. https://doi.org/10.1016/j.jseaes.2017.01.030

Tan, Y., & Helmberger, D. (2010). Rupture directivity characteristics of the 2003 Big Bear sequence. *Bulletin of the Seismological Society of America*, *100*(3), 1089–1106. https://doi.org/10.1785/0120090074

Waldhauser, F., & Ellsworth, W. L. (2000). A double-difference earthquake location algorithm: Method and application to the northern Hayward fault, California. *Bulletin of the Seismological Society of America*, *90*(6), 1353–1368. https://doi.org/10.1785/0120000006

Wang, M., Hubbard, J., Plesch, A., Shaw, J. H., & Wang, L. (2016). Three-dimensional seismic velocity structure in the Sichuan basin, China. *Journal of Geophysical Research: Solid Earth*, *121*, 1007–1022. https://doi.org/10.1002/2015JB012644

Wang, Q., & Chu, R. (2020). Earthquake source parameters in southwestern China and their rheological implications. *Seismological Research Letters*, *91*(2A), 936–947. https://doi.org/10.1785/0220190193

Wang, R. J., Lorenzo-Martín, F., & Roth, F. (2006). PSGRN/PSCMP—A new code for calculating co-and post-seismic deformation, geoid and gravity changes based on the viscoelastic-gravitational dislocation theory. *Computers & Geosciences*, *32*(4), 527–541. https://doi.org/10.1016/j.cageo.2005.08.006

Warren, L. M., & Silver, P. G. (2006). Measurement of differential rupture durations as constraints on the source finiteness of deep-focus earthquakes. *Journal of Geophysical Research*, *111*, B06304. https://doi.org/10.1029/2005JB004001

Weingarten, M., Ge, S., Godt, J. W., Bekins, B. A., & Rubinstein, J. L. (2015). High-rate injection is associated with the increase in US mid-continent seismicity. *Science*, *348*(6241), 1336–1340. https://doi.org/10.1126/science.aab1345

Wells, D. L., & Coppersmith, K. J. (1994). New empirical relationships among magnitude, rupture length, rupture width, rupture area, and surface displacement. *Bulletin of the Seismological Society of America*, *84*(4), 974–1002.

Yeck, W. L., Weingarten, M., Benz, H. M., McNamara, D. E., Bergman, E. A., Herrmann, R. B., et al. (2016). Far-field pressurization likely caused one of the largest injection-induced earthquakes by reactivating a large preexisting basement fault structure. *Geophysical Research Letters*, *43*, 10,198–10,207. https://doi.org/10.1002/2016GL070861

Yi, G., Long, F., Liang, M., Zhao, M., Wang, S., Gong, Y., et al. (2019). Focal mechanism solutions and seismogenic structure of the 17 June 2019 M$_S$6.0 Sichuan Changning earthquake sequence. *Chinese Journal of Geophysics* (in Chines), *62*(9), 3432–3447.

Zeng, Q., Chu, R., Sheng, M., & Wei, Z. (2020). Seismic ambient noise tomography for shallow velocity structures beneath Weiyuan, Sichuan. *Chinese Journal of Geophysics* (in Chines), *63*(3), 944–955.

Zeng, X., Xie, J., & Ni, S. (2015). Ground truth location of earthquakes by use of ambient seismic noise from a sparse seismic network: A case study in Western Australia. *Pure and Applied Geophysics*, *172*, 1397–1407.

Zhan, Z., Wei, S., Ni, S., & Helmberger, D. (2011). Earthquake centroid locations using calibration from ambient seismic noise. *Bulletin of the Seismological Society of America*, *101*(3), 1438–1445. https://doi.org/10.1785/0120100118

Zhao, Z., Fan, J., Zheng, S., Hasegawa, A., & Horiuchi, S. (1997). Precise modification of crustal velocity structure and source locations in Longmenshan fault zone. *Acta Seismologica Sinica (in Chinese)*, *19*(6), 615–622.

Zheng, X., Yao, Z., Liang, J., & Zheng, J. (2010). The role played and opportunities provided by IGP DMC of China National Seismic Network in Wenchuan earthquake disaster relief and researches. *Bulletin of the Seismological Society of America*, *100*(5B), 2866–2872. https://doi.org/10.1785/0120090257

Zhu, L., & Ben-Zion, Y. (2013). Parametrization of general seismic potency and moment tensors for source inversion of seismic waveform data. *Geophysical Journal International*, *194*(2), 839–843. https://doi.org/10.1093/gji/ggt137

Zhu, L., & Helmberger, D. V. (1996). Advancement in source estimation techniques using broadband regional seismograms. *Bulletin of the Seismological Society of America*, *86*(5), 1634–1641.

Zhu, L., & Rivera, L. A. (2002). A note on the dynamic and static displacements from a point source in multilayered media. *Geophysical Journal International*, *148*(3), 619–627. https://doi.org/10.1046/j.1365-246X.2002.01610.x

Zou, C., Yang, Z., Sun, S., Zhao, Q., Bai, W., Liu, H., et al. (2020). "Exploring petroleum inside source kitchen": Shale oil and gas in Sichuan Basin. *Science China Earth Sciences*, *63*(7), 934–953. https://doi.org/10.1007/s11430-019-9591-5